

Phase-only Image Based Kernel Estimation for Single-image Blind Deblurring

Liyuan Pan^{1,2}, Richard Hartley^{1,2}, Miaomiao Liu^{1,2}, and Yuchao Dai³

¹ Research School of Engineering, Australian National University, Canberra, Australia

² Australia Centre for Robotic Vision

³ School of Electronics and Information, Northwestern Polytechnical University, Xi'an, China

{liyuan.pan, Richard.Hartley, miaomiao.liu}@anu.edu.au, daiyuchao@nwpu.edu.cn

Abstract

The image blurring process is generally modelled as the convolution of a blur kernel with a latent image. Therefore, the estimation of the blur kernel is essentially important for blind image deblurring. Unlike existing approaches which focus on approaching the problem by enforcing various priors on the blur kernel and the latent image, we are aiming at obtaining a high quality blur kernel directly by studying the problem in the frequency domain. We show that the auto-correlation of the absolute phase-only image¹ can provide faithful information about the motion (e.g. the motion direction and magnitude, we call it the motion pattern in this paper.) that caused the blur; leading to a new and efficient blur kernel estimation approach. The blur kernel is then refined and the sharp image is estimated by solving an optimization problem by enforcing a regularization on the blur kernel and the latent image. We further extend our approach to handle non-uniform blur, which involves spatially varying blur kernels. Our approach is evaluated extensively on synthetic and real data and shows good results compared to the state-of-the-art deblurring approaches.

1. Introduction

Blind image deblurring aims at estimating the blur kernel and the latent image from an input blurry image. This is an ill-posed problem as there are infinitely many pairs of blur kernels and images that could generate the same blurry image. Blind image deblurring has been extensively studied in computer vision and is still a very active research area [10, 29, 6, 27, 20, 35], where blur kernel estimation is essentially important in obtaining a high quality sharp image.

Existing blind image deblurring methods tend to formulate the problem within the Maximum A Posteriori (MAP)

framework, where the blur kernel and the latent sharp image are optimized jointly. To resolve the ill-posed underlining optimization problem, various assumptions, or regularizations, have been proposed for the blur kernel and the desired latent image, such as the dark channel prior [25], extreme channel prior [44], l_0 regularized prior [23, 42], learned image prior using a CNN [18], uniform blur [17, 43], non-uniform blur from multiple homographies [8, 22], constant depth [7, 40], in-plane rotation [33], and forward motion [46]. The resultant optimization problem is non-convex in general. The blur kernel and the latent image are usually solved in an alternating fashion. Thus, a proper and effective initialization is demanded to achieve a good *local optimum solution* and makes the algorithm converge quickly.

In his paper, we aim at estimating a high-quality blur kernel directly from the input blurry image by studying the problem in the frequency domain. We exploit the *phase-only image* of the input blurry image, which is reconstructed from the Fourier transformed image using the phase information only. The *phase-only image* contains edge and texture information about the image structure [21, 28]. The motion (either camera or object motion) information is encoded as repeated image edges in the *phase-only image* (see Fig. 1 for an example). We show that the auto-correlation of the absolute *phase-only image* reveals the motion information including the motion direction and motion magnitude, which is referred to as the *motion pattern* in this paper. It provides information about the blur kernel, thereby leading to a new approach to estimating the blur kernel.

We further improve the blur kernel and latent image estimation by enforcing a spatial sparsity prior on the kernel as well as the latent image gradient in a simple optimization framework. Furthermore, our blur kernel estimation approach can be naturally extended to handle non-uniform blur in order to deal with the spatially-variant blur kernels that arise in complex image deblurring problems. Extensive experiments on both synthetic and real images demonstrate the superiority of our approach over the state-of-the-art methods.

¹Phase-only image means the image is reconstructed only from the phase information of the blurry image.

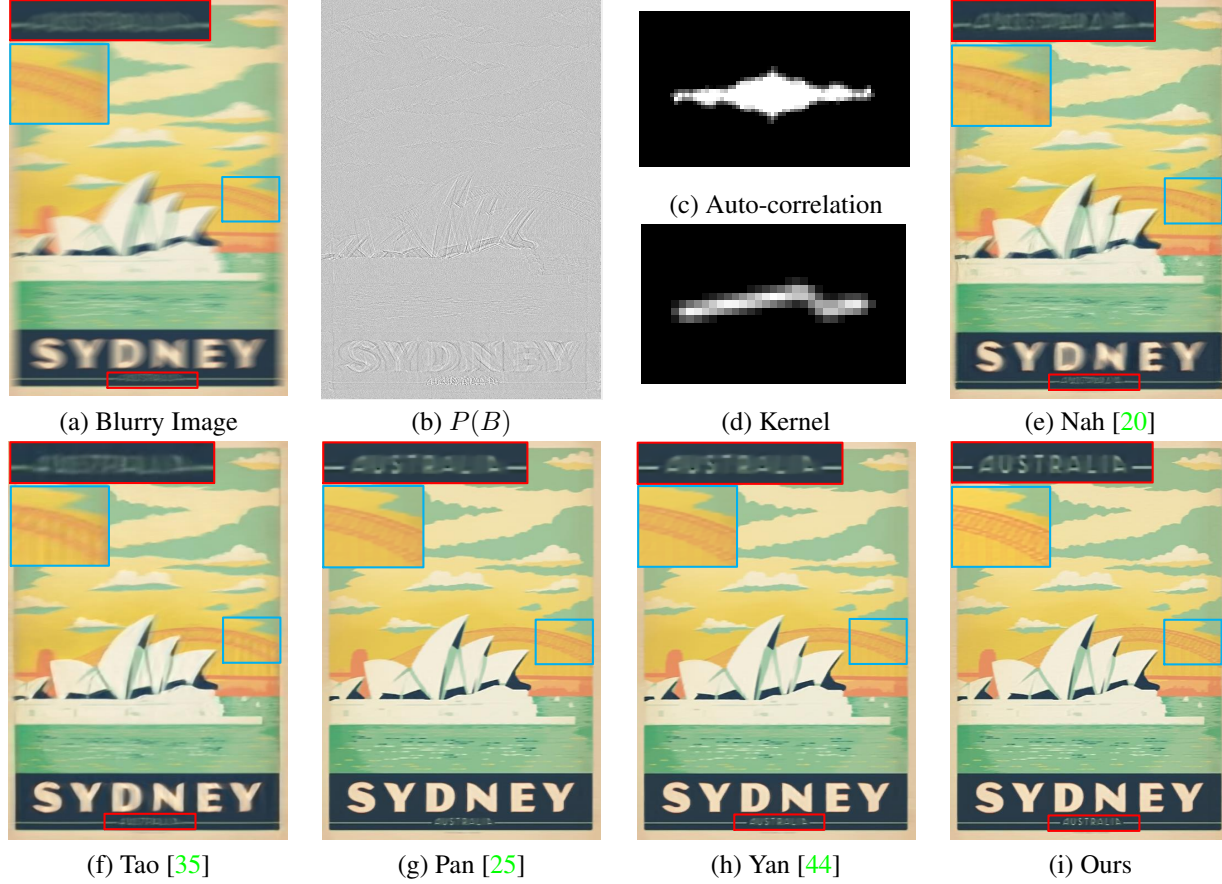


Figure 1. Our deblurring result compared with the state-of-the-art methods. (a) Input blurry image. (b) The phase-only image. (c) The auto-correlation for the phase-only image. (d) The estimated blur kernel. (e) Deblurring result of [20]. (f) Deblurring result of [35]. (g) Deblurring result of [25]. (h) Deblurring result of [44]. (i) Our deblurring result. (Best viewed on screen).

Our main contributions are summarized as follows

- 1) We propose a new *phase-only image*-based approach to directly estimating the blur kernel from the input blurry image. The approach for *motion pattern* estimation is easy and efficient, consisting of a few lines of code.
- 2) Our single-image blind deblurring model can be naturally extended to handle non-uniform blur in an effective manner. Furthermore, the estimated blur kernel can be easily refined by only enforcing spatial sparsity.
- 3) Evaluated on both synthetic and real images, our proposed approach shows impressive results compared to other state-of-the-art blind deblurring approaches.

2. Related Work

Single-image blind deblurring. Single-image deblurring jointly estimates the blur kernel and the latent sharp image from the blurry one, which is highly under-constrained since the blurry image could be explained by many pairs of blur kernel and sharp image [14, 24]. In general, image deblurring is formulated in a MAP framework with *priors* on blur kernels or latent images. The Sparsity prior has

proved effective in blur kernel estimation. For instance, Krishnan *et al.* [15] applied normalized sparsity in their MAP framework to estimate the blur kernel. Xu *et al.* [43] proposed an approximation of the l_0 -norm as a sparsity prior in order to jointly estimate sharp image and blur kernels. Edge-based methods for blur kernel estimation have been exploited recently [39, 11, 3, 34]. Xu *et al.* [39] proposed a two-phase method for single-image deblurring. The blur kernel is first estimated based on the selected image edges and refined by ISD optimization. The latent sharp image is then restored by total-variation (TV)- l_1 deconvolution. In addition, a Gaussian prior is imposed to help the estimation of the blur kernel [11, 3], which leads to an efficient solver. Moreover, the blur kernel has been modelled based on various motion assumptions, such as in-plane camera rotation [33] or camera forward motion [46]. A few works have exploited the layer-wise scene structure to model the blur kernel [7, 8, 22]. For example, Gupta *et al.* [7] represent the camera motion trajectory using a motion density function, which requires a constant depth or fronto-parallel scene assumption. Hu *et al.* [8] proposed jointly estimat-

ing the depth layering and remove the blur caused by in-plane motion from a single blurry image. Pan *et al.* [22] proposed jointly estimating object segmentation and camera motion by incorporating soft segmentation. Note that both approaches require user input for initial depth layer segmentation.

Video image blind deblurring. In order to better model non-uniform blur, monocular video and stereo based deblurring approaches are proposed to handle blurring in realistic scenes. Cho *et al.* [5] proposed a method relying on the assumption that salient sharp frames frequently exist in videos, which only allows for slowly moving objects in dynamic scenes. Wulff and Black [38] proposed a layered model to estimate both foreground motion and background motion. However, these motions are restricted to affine models, and it is difficult to extended them to multi-layer scenes due to the difficulty in depth ordering. Kim and Lee [9] incorporated optical flow estimation to guide the blur kernel estimation, which is able to deal with certain object motion blur. In [10], a new method is proposed to simultaneously estimate optical flow and tackle general blur by minimizing a single non-convex energy function. Stereo images and videos can provide depth information which allows to better model pixel-wise blur kernel. Recently, Sellent *et al.* [29] proposed a stereo video deblurring technique, where 3D scene flow is estimated from the blurry images using a piecewise rigid scene representation. Pan *et al.* [27] proposed a single framework to jointly estimate the scene flow and deblur the images.

Deep learning based image deblurring. Recently, image deblurring has greatly benefited from the great advances in deep learning [16, 33, 45, 35]. Sun *et al.* [33] proposed a convolutional neural network (CNN) to estimate locally linear blur kernels. Gong *et al.* [6] learned optical flow field from a single blurry image directly through a fully-convolutional deep neural network. The blur kernel is then obtained from the estimated optical flow which is applied in an MAP framework to restore the sharp image. Su *et al.* [32] trained an end-to-end CNN to accumulate information across frames for video deblurring. Nah *et al.* [20] proposed a multi-scale CNN that restores latent images in an end-to-end learning manner without any assumption on the blur kernel model. Li *et al.* [18] used a learned image prior to distinguish whether an image is sharp or not and embedded the learned prior into the MAP framework. Tao *et al.* [35] proposed a light and compact network, SRN-DeblurNet, to deblur the image. While achieving reasonable performance on various scenarios, the success of these deep learning based methods depends on the consistency between the training datasets and the testing datasets, which can hinder the generalization ability.

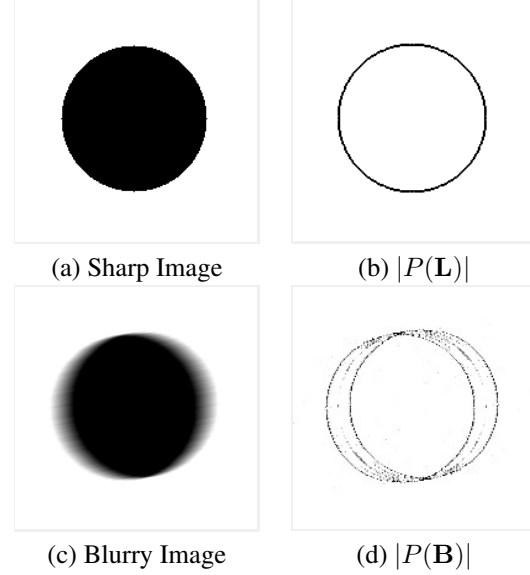


Figure 2. We use a circle image as an example. The image is blurred by a linear kernel, where the kernel length is 20 pixels and the direction is 10 degree.

3. Method

3.1. Fourier Theory of Phase-only Images

This section contains the main theoretical insights of this paper. Our goal is to find the latent sharp image from a single blurry image. The blurry image can be modelled as a convolution of the latent image with a blur kernel,

$$\mathbf{B} = \mathbf{L} \otimes \mathbf{k}, \quad (1)$$

where \mathbf{B} is the known blurry image, \mathbf{L} denotes the latent sharp image, \mathbf{k} is the blur kernel, \otimes is the convolution operator. Note that this problem is highly under-determined since multiple pairs of \mathbf{L} and \mathbf{k} can lead to the same blurry image.

In the Fourier domain, Eq. (1) corresponds to $\mathcal{F}(\mathbf{B}) = \mathcal{F}(\mathbf{L}) \odot \mathcal{F}(\mathbf{k})$, where \odot represents the component-wise multiplication.

The phase and amplitude of a complex number $z = ke^{i\theta}$ are $e^{i\theta}$ and $k \geq 0$ respectively. Applying these component-by-component to a Fourier transformed image $\mathcal{F}(\mathbf{L})$ gives the phase and amplitude components. We denote taking the phase of a complex signal by $\mathcal{P}(\cdot)$. Taking the inverse Fourier transform of the phase-component gives the *phase-only image*, $P(\mathbf{L}) = \mathcal{F}^{-1}(\mathcal{P}(\mathcal{F}(\mathbf{L})))$. It is well known that the phase-only image bears more similarity to the original image than the analogously defined amplitude image. Fig. 2 shows an example of the phase-only image derived from a clean and blurry image. As may be observed, taking a phase-only image acts as a sort of edge-extractor. This is related to the fact, noted in [13] that the Fourier components

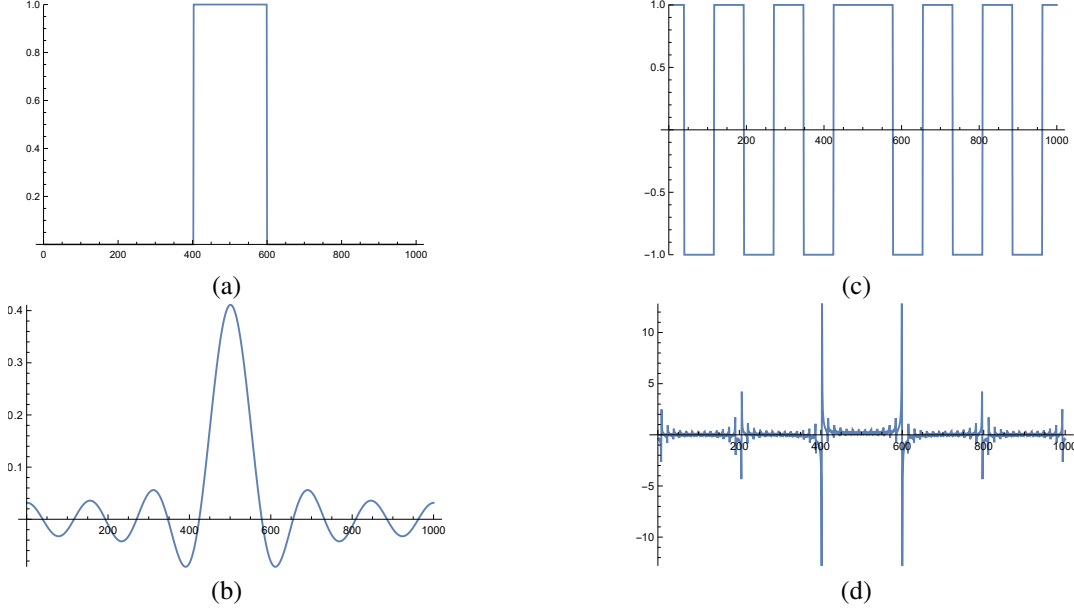


Figure 3. Given a top-hat function (a), its Fourier transform is a sinc shown in (b). (The central peak has twice the width of the others. Note that since the top-hat is symmetric, its Fourier transform is real, hence its phase is either +1 or -1 shown in (c).) The phase-only image of the top-hat shown in (d) is obtained by taking the inverse Fourier transform of the function in (c).

of an edge tend to be in-phase with each other. For a real image \mathbf{L} , the phase-only image will also be real. Another simple property is *rotation-covariance*: if R represents rotation then $P(R(\mathbf{L})) = R(P(\mathbf{L}))$. It is also shift-covariant.

We now make a basic observation regarding the phase-only image of a convolution.

lemma 1. *The phase-only image of a convolution $P(\mathbf{L} \otimes \mathbf{k})$, equals the convolution of the phase-only image and the phase-only kernel.*

$$P(\mathbf{L} \otimes \mathbf{k}) = \mathcal{F}^{-1}(\mathcal{P}(\mathcal{F}(\mathbf{L} \otimes \mathbf{k}))) = P(\mathbf{L}) \otimes P(\mathbf{k}). \quad (2)$$

This results from a simple calculation.

Linearly-blurred image. For a simple linear (straight-line) blur kernel, the form of $P(\mathbf{k})$ can be computed. By rotation and shift covariance, it may be assumed without loss of generality, that \mathbf{k} is axis-aligned, in which case $\mathbf{k}(x, y) = \delta(y)H(x)$, where $\delta(y)$ is a Dirac delta function and $H(x)$ is a top-hat. The Fourier transform is separable, so it follows that $P(\mathbf{k})(x, y) = \delta(y)P(H)(x)$. Hence, we investigate what the 1D phase-only signal $P(H)$ is. The result is shown in Fig. 3. A formula for the shape of the phase-only top-hat of width w is derived (for the continuous Fourier Transform) in the supplementary material, and is equal to $(\sqrt{2\pi}/w) \text{sinc}(\pi x/w) / \cos(\pi x/w)$, which is plotted in Fig. 3(d). More details of the properties of this function are given in the supplementary material.

According to Eq. (2), if $\mathbf{B} = \mathbf{L} \otimes \mathbf{k}$, then $P(\mathbf{B})$ is obtained by convolving $P(\mathbf{L})$ in the orientation of the linear

kernel with the phase-only kernel, shown in Fig. 3(d). This results in the creation of multiple copies (“ghosts”), of the phase-only image, $P(\mathbf{L})$, separated by the width of the filter. (The copies due to the principal peaks will be the most noticeable.)² This is shown in Fig. 4.

The key advantage of phase-only image. This analysis and the examples show the advantage and purpose in considering the phase-only image as a means of determining the blur kernel, and subsequently deblurring the image. This is illustrated by the analysis of the linear kernel.

The effect of blurring is to smear the image in the blur direction, as shown in Fig. 4 (top left). From this image, it is not easy to discern the shape of the kernel, particularly the linear extent of the kernel. On the other hand, in the phase-only image, the effect of blurring is to create *two principal identical copies* of $P(\mathbf{L})$ separated by the extent of the blur kernel. This is immediately evident from Fig. 4(b), or Fig. 2(d). Thus, the continuous smear in the blurred image is replaced by a simple sum of two (principle) copies in the phase-only blurred image. This simplification of the effect of blurring makes the further image-processing to compute the blur-kernel much simpler.

This discovery of the application of the phase-only image to deblurring is the key original contribution of this paper, and the supplementary material provides a rigorous mathematical justification of the empirical observation,

² A more exact statement is that $P(\mathbf{B})$ consists of multiple ghosts, separated by the filter width, of the **gradient** of $P(\mathbf{L})$ in the filter direction. An exact derivation is given in the supplementary material. This includes also an exact derivation of $P(H)$.

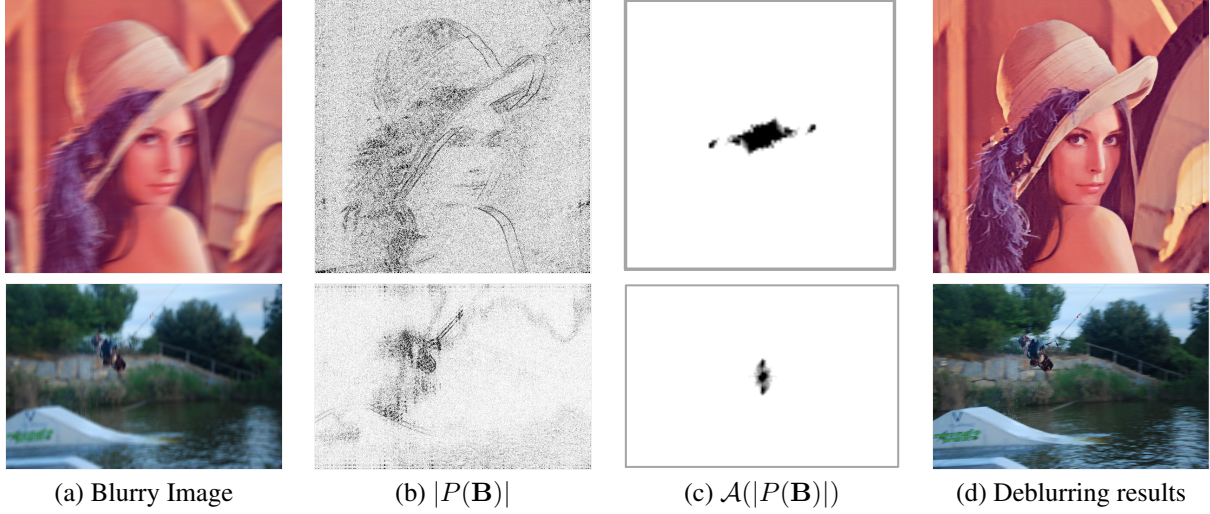


Figure 4. (a) Input blurry images, the top one is a synthetic image created by ourselves and the bottom one is a real image from dataset [30]. (b) The absolute phase-only image of the blurry image, $|P(\mathbf{B})|$, results in two principal copies (others more faint) of $P(\mathbf{L})$. (c) The autocorrelation of the absolute phase-only image, $\mathcal{A}(|P(\mathbf{B})|)$, showing two distinct peaks (separated by the length of the filter kernel). Distinguishing the two principal peaks of the autocorrelation (apart from the origin) can be used to determine the orientation and width of a linear (straight-line) blur kernel. (d) shows our deblurring results with sharp edges.

which we hope the reader will enjoy.

3.2. Autocorrelation

Using phase-only to obtain $P(\mathbf{B})$ from a blurry image results in multiple (two principal) shifted copies of $P(\mathbf{L})$. Note that $P(\mathbf{L})$ is not known. However, this suggests the use of autocorrelation of $P(\mathbf{B})$.

Autocorrelation of a signal \mathbf{I} (1 or 2-dimensional) is computed using Fourier transform as:

$$\mathcal{A}(\mathbf{I}) = \mathcal{F}^{-1}(\mathcal{F}(\mathbf{I}) \odot \overline{\mathcal{F}(\mathbf{I})}).$$

Unfortunately, if \mathbf{I} is itself a phase-only image, derived from \mathbf{J} , then

$$\mathcal{F}(\mathbf{I}) = \mathcal{F}(\mathcal{F}^{-1}\mathcal{P}(\mathcal{F}(\mathbf{J}))) = \mathcal{P}(\mathcal{F}(\mathbf{J})).$$

So $\mathcal{A}(\mathbf{I}) = \mathcal{F}^{-1}(\mathcal{P}(\mathcal{F}(\mathbf{J})) \odot \overline{\mathcal{P}(\mathcal{F}(\mathbf{J}))}) = \mathcal{F}^{-1}(1) = \delta$ where δ is a Dirac delta function at the origin. In other words, a phase-only image is **completely un-selfcorrelated**.

In other words, we cannot derive any information whatever from the autocorrelation of a phase-only image. The solution is to use the absolute value of the phase-only image instead. In other words, we compute $\mathcal{A}(|P(\mathbf{B})|)$, which should show the desired behaviour.

Fig. 4 shows the absolute *phase-only image* $|P(\mathbf{B})|$ and its autocorrelation $\mathcal{A}(|P(\mathbf{B})|)$. It is noticed that multiple copies of $|P(\mathbf{L})|$ are shown in $|P(\mathbf{B})|$. The most noticeable repeated edges are due to the principal peak of $P(\mathbf{k})$ (as analyzed above) indicating the start and end point of the moving camera.

The autocorrelation of the absolute *phase-only image* shows several bright points that indicate the motion of the camera, e.g. the motion direction and magnitude, which is referred to as *motion pattern*. The autocorrelation image will consist of a central peak plus two side-peaks separated by the extent (and in the direction) of the blur-kernel.

Consequently, the motion of the camera will provide faithful information for obtaining the blur kernel. Therefore, in the following section, we will present our approach to image deblurring based on the analysis of the autocorrelation of the absolute *phase-only image*.

4. Uniform Deblurring

Based on the analysis of the Fourier theory of phase-only images, we introduce our approach to estimate the blur kernel and deblur the images.

4.1. Uniform Blur from Linear Motion

Consider the blur caused by a pure linear motion. By computing the autocorrelation of the absolute *phase-only image*, the *motion pattern*, namely the motion direction and the motion magnitude, is extracted by directly connecting the two end bright points in $\mathcal{A}(|P(\mathbf{B})|)$. The blur kernel is then formed based on the extracted *motion pattern*. In particular, the motion magnitude determines the kernel size. The non-zero kernel values are uniformly distributed along the motion direction (see Fig. 4 the top row for an example). Given the built blur kernel, the latent image can be easily obtained by solving the Eq. (3) which will be introduced in the following section.

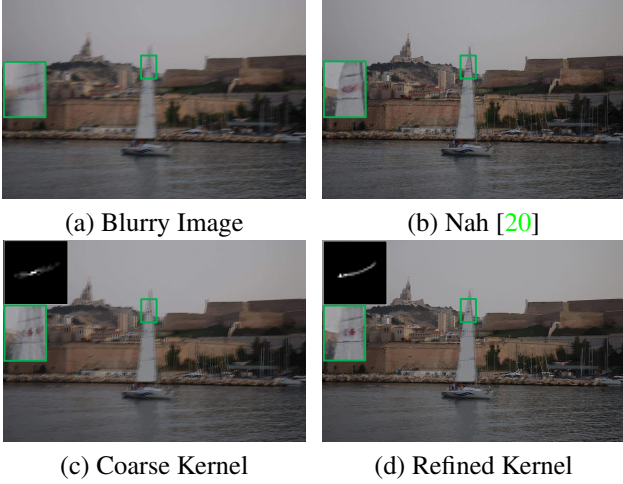


Figure 5. (a) The blurry image from dataset [25]. (b) Deblurring results of [20]. (c) Our deblurring result with the coarse blur kernel built from the autocorrelation of the absolute phase-only image. (d) Our deblurring result with the refined kernel. The refined kernel can better improve the deblurring result by looking at the close-up of the part of the sail with detailed sharp edges. Note that the blur kernel is zoomed in the corner.

4.2. Uniform Blur from Complex Motion

The blurry image is formed by the integral of light intensity over the exposure period. For more complex motion, the autocorrelation image $\mathcal{A}(|P(\mathbf{B})|)$ will show more bright points representing high correlation values (see Fig. 1 (c) and Fig. 4 (c) for examples).

In general, in the case of uniform (spatially-invariant) blur, one may write $\mathbf{B} = \mathbf{k} \otimes \mathbf{L}$, so, allowing for the possibility of noise, the deblurring problem (with known kernel) may be formulated as finding $\arg\min_{\mathbf{L}} \|\mathbf{k} \otimes \mathbf{L} - \mathbf{B}\|_2^2$. In most cases, however, blurring acts as a form of low-pass filter – high-frequency information is lost. Consequently, this problem is not well-conditioned. Thinking of convolution with known \mathbf{k} as being a linear operator, there exist near-zero eigenvalues whose eigenvectors correspond to high-frequency components of the signal (image). The deblurring process is to restore the lost frequency components of the image. If high-frequency components are over-emphasized in the deblurring process, the resulting latent image \mathbf{L} will be noisy, or edges will show ringing. A common solution to this is to add a regularization term that discourages excessive high-frequency components. One is therefore led to the following minimization problem.

$$\min_{\mathbf{L}} \|\mathbf{k} \otimes \mathbf{L} - \mathbf{B}\|_2^2 + \mu_2 h(\nabla \mathbf{L}), \quad (3)$$

where $h(\cdot)$ is a penalty term used to discourage excessive gradients, which are indicative of noise and over-emphasized edges.

In the case of complex motion, the kernel is not known exactly, but an initial value of \mathbf{k} may be estimated directly from the autocorrelation of the absolute *phase-only image* as described previously. Our final goal is to further refine the kernel \mathbf{k} and estimate the latent sharp image \mathbf{L} by solving

$$\min_{\mathbf{L}, \mathbf{k}} \|\mathbf{k} \otimes \mathbf{L} - \mathbf{B}\|_2^2 + \mu_1 \|\mathbf{k}\|_2^2 + \mu_2 h(\nabla \mathbf{k}), \quad (4)$$

where μ_1 and μ_2 are weight parameters. The first term encodes the fact that the modelled blurry image should be similar to the observed image. The second term is to regularize the solution of the blur kernel. The third term prevents over-sharpening.

The optimization of our energy function defined in Eq. (4) involves two sets of variables, the kernel and the latent image. We perform the minimization iteratively starting with the initial estimate of \mathbf{k} given by the phase-only technique. (See Fig. 5 for an example).

4.2.1 Estimating the Latent Image

The goal is to minimize Eq. (4) by alternation. If \mathbf{k} is known, the problem comes down to minimizing Eq. (3).

Specifically, we use a truncated-quadratic gradient regularization term

$$h(\nabla \mathbf{L}) = \sum_{x,y} \min(\|\nabla_{xy} \mathbf{L} / \epsilon\|^2, 1)$$

where $\epsilon \in [0.1, 1]$ and $\nabla_{xy} \mathbf{L}$ represents the gradient of \mathbf{L} at image coordinates (x, y) . This regularization term smooths out small noise, while allowing occasional large gradients (intensity differences). This type of term, proposed by [2] is widely used to regularize noise and gradients in stereo [36] and was also used in deblurring in [43]). Because the truncated quadratic is non-convex, the optimization problem is non-convex. We use the method of half quadratic splitting, as in [41], to minimize this cost function, though other methods such as Iterative Reweighted Least Squares could be used for such truncated-quadratic cost [1].

4.2.2 Refining the Kernel

Now, with \mathbf{L} known, the motion blur kernel can be refined by solving

$$\min_{\mathbf{k}} \|\mathbf{k} \otimes \mathbf{L} - \mathbf{B}\|_2^2 + \mu_1 \|\mathbf{k}\|_2^2.$$

This is a quadratic problem, and can be solved directly by taking gradients, which results in a set of linear equations. More efficiently, we solve it in the Fourier domain, in which case there is a closed-form solution

$$\mathcal{F}(\mathbf{k}) = \overline{\mathcal{F}(\mathbf{L})} \odot \mathcal{F}(\mathbf{B}) / (\overline{\mathcal{F}(\mathbf{L})} \odot \mathcal{F}(\mathbf{L}) + \mu_1),$$

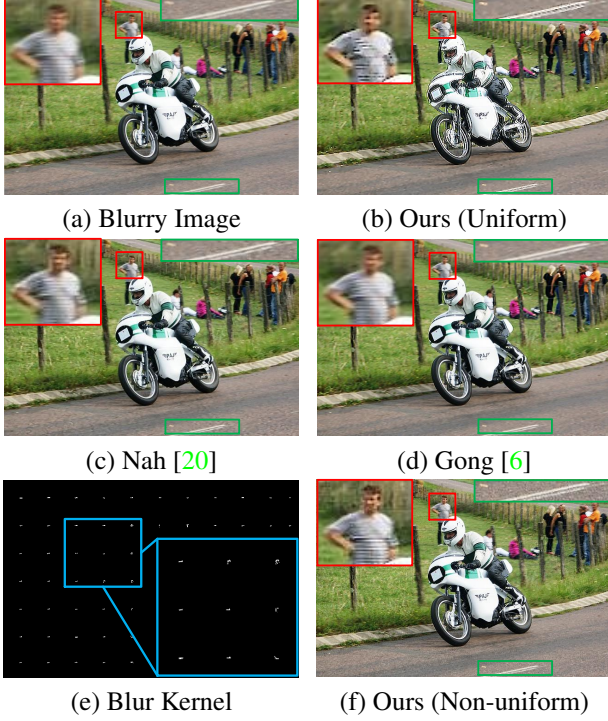


Figure 6. Example of our non-uniform blur kernel where the real blurry image is from [6]. (a) Input blurry image. (b) Our deblurring results by using uniform blur model and its blur kernel. We can see clearly that the man in a plaid shirt seems not deblurred because of the improper kernel. (c) Deblurring result of [20]. (d) Deblurring result of [6]. (e) Non-uniform blur kernel. (f) Our deblurring result by using non-uniform blur model and kernel.

where the division is carried out point-wise (as are the multiplications). Then \mathbf{k} is found by the inverse transform, and then normalized to sum to 1.

The algorithm alternates between recomputing \mathbf{L} and \mathbf{k} until convergence, or for a fixed number of steps.

5. Extension to Non-uniform Deblurring

Our method can be easily extended to handle non-uniform blur (e.g., the background and foreground undergo different blur) by deblurring the image patch-by-patch or layer-by-layer. Each patch or layer of the image corresponds to a different blur kernel. The new non-uniform blur model can be expressed as

$$\mathbf{B} = \sum_{i=1}^N \mathbf{k}_i \otimes \mathbf{l}_i, \quad (5)$$

where N denotes the number of segmented patches or layers, $\mathbf{l}_i = \mathbf{M}_i \odot \mathbf{L}$ is to extract the i -th patch or layer of the latent image, \mathbf{M}_i is a binary mask with non-zeros values in the region corresponding to the i -th patch or layer in \mathbf{L} , and \mathbf{k}_i denotes the blur kernel corresponding to the i -th patch. Similarly, we define $\mathbf{B}_i = \mathbf{k}_i \otimes \mathbf{l}_i$ and $\mathbf{B} = \sum_{i=1}^N \mathbf{B}_i$.

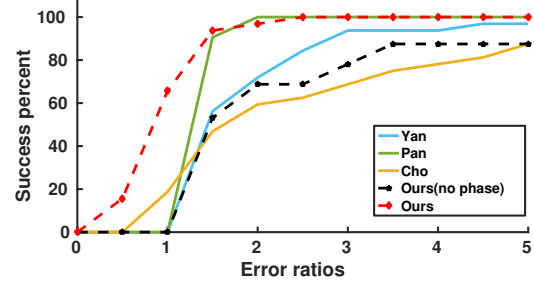


Figure 7. Quantitative evaluations on dataset [17]. We report the experimental results with and without using the blur kernel estimated from the phase-only image ('Ours(no phase)'). The results further demonstrate the effectiveness of blur kernel estimation from the phase-only image.

Table 1. Quantitative comparison on the dataset [17].

	Cho [4]	Pan [25]	Yan [44]	Our (no phase)	Our
PSNR(dB)	25.63	27.54	24.70	25.74	28.38
SSIM	0.7907	0.8626	0.8760	0.7842	0.9250
SSD	2.6688	1.2747	1.6802	3.2517	0.8776

Each layer can be handled using our proposed uniform deblurring approach in Section 4. The final latent image \mathbf{L} is $\sum_{i=1}^N \mathbf{l}_i$. In Fig. 6, we give an example of the deblurring results for uniform and non-uniform blur models. The image is a real blurry image from dataset [6]. Clearly, our non-uniform deblurring achieves better results than our uniform-deblurring model and the other existing non-uniform deblurring methods which either use additional depth, camera pose information [8, 7, 37] or use deep convolutional neural networks [6, 20].

6. Experiments

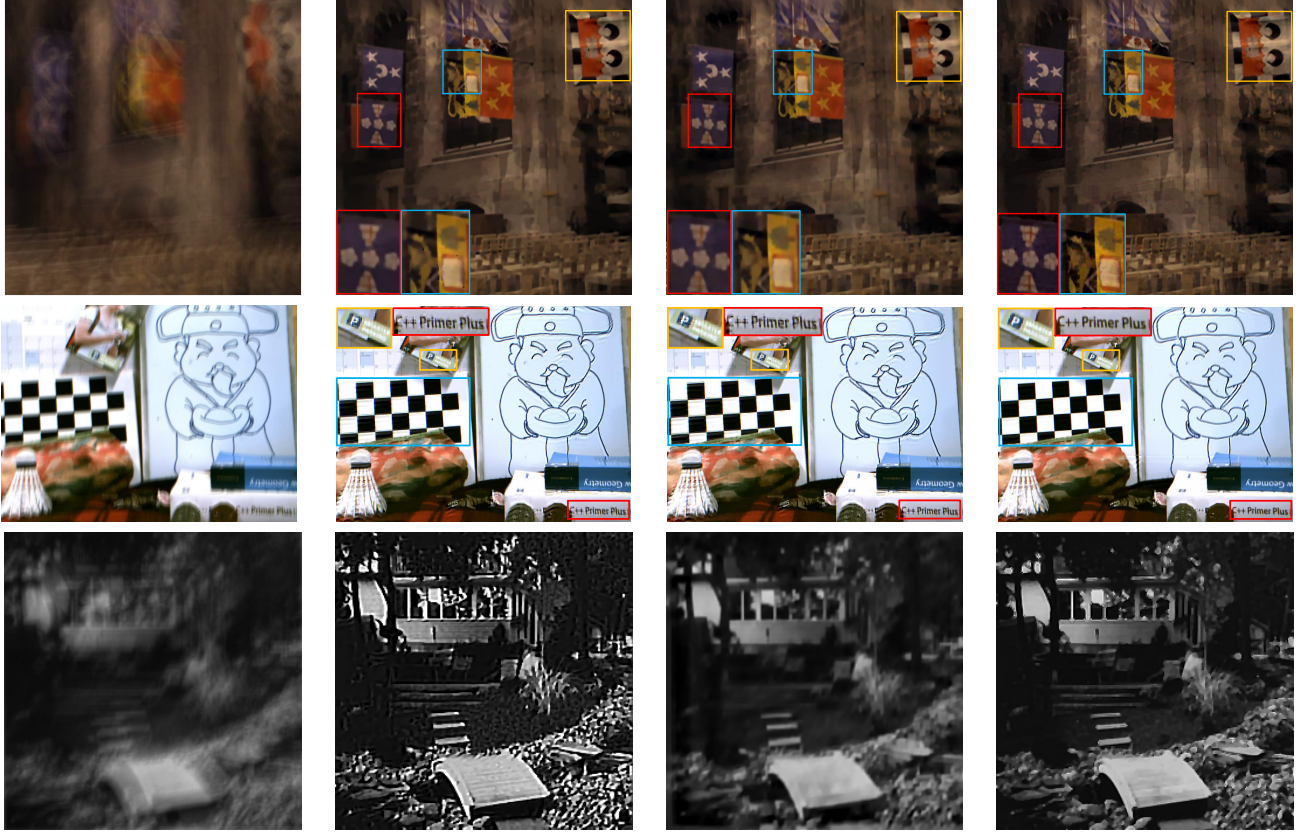
6.1. Experimental Setup

Dataset. We evaluate our approach on the datasets provided by [12, 25, 31, 6, 17] and images captured by ourselves, which covers images from man-made scene, natural scene and images containing text (see Fig. 5, 6, 8 for examples).

Baselines and evaluation metric. Since our proposed approach can handle both uniform and non-uniform blurs, we compare with state-of-the-art methods for both cases separately. For traditional methods (non-deep learning methods), we compare with [44, 25, 3, 37, 43]. For deep learning based methods, we compare with [6, 20, 16] which can handle spatially-variant blur. We report the PSNR, SSIM on datasets [17, 12] and *error ratio*³ on dataset [17] which provides the ground truth blur kernels for evaluation.

Implementation details. We validate the parameters in our model on three reserved images for each dataset and use

³ *Error ratio* is introduced in [17] which measures the ratio between the SSD (Sum of Squared Distance) of the deconvolution error computed with the estimated kernel and the ground truth kernel.



(a) Blurry Image

(b) Yan [44]

(c) Pan [25]

(d) Ours

Figure 8. *Qualitative comparison on example images from dataset [12](top), [17](bottom) and image taken by ourselves (middle). (a) Input blurry images. (b) Deblurring results of [44]. (c) Deblurring results of [25]. (d) Our deblurring result. (Best viewed on screen).*

Table 2. *Quantitative comparisons on the dataset [12], where [20, 16] are deep based methods.*

	Blurry Image	Whyte <i>et al.</i> [37]	Xu <i>et al.</i> [43]	Pan <i>et al.</i> [25]	Yan <i>et al.</i> [44]	Nah <i>et al.</i> [20]	Kupyn <i>et al.</i> [16]	Ours
PSNR(dB)	24.93	27.03	27.47	29.95	28.42	26.48	26.10	30.18
SSIM	0.783	0.809	0.811	0.932	0.897	0.807	0.816	0.933

coarse-to-fine strategy for deblurring. We set $\mu_1 = 2$, $\mu_2 = 0.005$ for our experiments. Our framework is implemented using MATLAB with C++ wrappers. It takes around 40 second to process one image (800×800) on a single i7 core running at 3.6 GHz.

6.2. Experimental Results

The dataset introduced in [17] is a widely used uniform blur dataset, which contains 32 blurry images generated by 4 ground truth images and 8 blur kernels. We perform the quantitative and qualitative evaluation on this dataset. Results are shown in Fig. 7, 8 and Table 1, which demonstrates that our proposed approach achieves competitive results.

The *Natural dataset* is generated by [12] with camera motion measured and controlled by a Vicon tracking system. Specifically, the dataset provides blurry image, its latent image, and ground truth blur kernel, which allows the quantitative comparison of our approach with baselines.

The captured images are of size 800×800 . In Table 2, we show the quantitative comparison with the state-of-the-art Single-image deblurring approaches on dataset [12]. It demonstrates that our approach can achieve the best performance on the PSNR and SSIM score.

We further show the corresponding qualitative comparison results on example images in [12] in Fig. 8. It clearly shows that our approach can recover more sharp details and with less ringing artifacts than other approaches, which are highlighted in the presented results. We also report our deblurring result in Fig. 1, 4, 5 and 6, respectively. Note that our deblurring results can recover the color more faithfully than the baselines. In order to show the effectiveness of our approach on the results of other subsequent tasks, we also perform a detailed analysis on visual SLAM on the TUM [31] ‘Teddy’ dataset. The analysis as well as more deblurring results are included in the supplementary material.

7. Conclusions

Our proposed *phase-only image* based kernel estimation approach is simple (implemented in a few lines of code). The resulted image deblurring algorithm achieves better quantitative results (using PSNR, SSIM, and SSD), than the state-of-the-art methods by extensive evaluation on the benchmark datasets. While our approach can handle the general blur cases, it still suffers from low lighting condition like other deblurring methods. Our future work will explore how to remove blurs less sensitive to lighting conditions.

References

- [1] K. Aftab and R. Hartley. Convergence of iteratively re-weighted least squares to robust m-estimators. In *Applications of Computer Vision (WACV), 2015 IEEE Winter Conference on*, pages 480–487. IEEE, 2015. 6
- [2] A. Blake and A. Zisserman. *Visual Reconstruction*. MIT Press, Cambridge, MA, USA, 1987. 6
- [3] S. Cho and S. Lee. Fast motion deblurring. *ACM Trans. Graph.*, 28:145:1–145:8, 2009. 2, 7
- [4] S. Cho, J. Wang, and S. Lee. Handling outliers in non-blind image deconvolution. In *Proc. IEEE Int. Conf. Comp. Vis.*, pages 495–502. IEEE, 2011. 7
- [5] S. Cho, J. Wang, and S. Lee. Video deblurring for hand-held cameras using patch-based synthesis. *ACM Transactions on Graphics (TOG)*, 31(4):64, 2012. 3
- [6] D. Gong, J. Yang, L. Liu, Y. Zhang, I. Reid, C. Shen, A. van den Hengel, and Q. Shi. From motion blur to motion flow: A deep learning solution for removing heterogeneous motion blur. In *Proc. IEEE Conf. Comp. Vis. Patt. Recogn.*, pages 2319–2328, 2017. 1, 3, 7
- [7] A. Gupta, N. Joshi, C. L. Zitnick, M. Cohen, and B. Curless. Single image deblurring using motion density functions. In *Proc. Eur. Conf. Comp. Vis.*, pages 171–184. Springer, 2010. 1, 2, 7
- [8] Z. Hu, L. Xu, and M.-H. Yang. Joint depth estimation and camera shake removal from single blurry image. In *Proc. IEEE Conf. Comp. Vis. Patt. Recogn.*, pages 2893–2900, 2014. 1, 2, 7
- [9] T. Hyun Kim and K. M. Lee. Segmentation-free dynamic scene deblurring. In *Proc. IEEE Conf. Comp. Vis. Patt. Recogn.*, pages 2766–2773, 2014. 3
- [10] T. Hyun Kim and K. Mu Lee. Generalized video deblurring for dynamic scenes. In *Proc. IEEE Conf. Comp. Vis. Patt. Recogn.*, pages 5426–5434, 2015. 1, 3
- [11] N. Joshi, R. Szeliski, and D. J. Kriegman. Psf estimation using sharp edge prediction. In *Proc. IEEE Conf. Comp. Vis. Patt. Recogn.*, pages 1–8, 2008. 2
- [12] R. Köhler, M. Hirsch, B. Mohler, B. Schölkopf, and S. Harmeling. Recording and playback of camera shake: Benchmarking blind deconvolution with a real-world database. In *Proc. Eur. Conf. Comp. Vis.*, pages 27–40. Springer, 2012. 7, 8, 14, 16, 17, 18, 19
- [13] P. Kovesi. Phase congruency detects corners and edges. In *DICTA*, 2003. 3, 11
- [14] D. Krishnan and R. Fergus. Fast image deconvolution using hyper-laplacian priors. In *Proc. Adv. Neural Inf. Process. Syst.*, pages 1033–1041, 2009. 2
- [15] D. Krishnan, T. Tay, and R. Fergus. Blind deconvolution using a normalized sparsity measure. In *Proc. IEEE Conf. Comp. Vis. Patt. Recogn.*, pages 233–240, 2011. 2
- [16] O. Kupyn, V. Budzan, M. Mykhailych, D. Mishkin, and J. Matas. Deblurgan: Blind motion deblurring using conditional adversarial networks. *ArXiv e-prints*, 2017. 3, 7, 8
- [17] A. Levin, Y. Weiss, F. Durand, and W. T. Freeman. Understanding and evaluating blind deconvolution algorithms. In *Proc. IEEE Conf. Comp. Vis. Patt. Recogn.*, pages 1964–1971, 2009. 1, 7, 8
- [18] L. Li, J. Pan, W.-S. Lai, C. Gao, N. Sang, and M.-H. Yang. Learning a discriminative prior for blind image deblurring. In *Proc. IEEE Conf. Comp. Vis. Patt. Recogn.*, pages 6616–6625, 2018. 1, 3
- [19] R. Mur-Artal and J. D. Tardós. ORB-SLAM2: an open-source SLAM system for monocular, stereo and RGB-D cameras. *IEEE Transactions on Robotics*, 33(5):1255–1262, 2017. 15
- [20] S. Nah, T. H. Kim, and K. M. Lee. Deep multi-scale convolutional neural network for dynamic scene deblurring. In *Proc. IEEE Conf. Comp. Vis. Patt. Recogn.*, July 2017. 1, 2, 3, 6, 7, 8, 16, 17, 18, 19
- [21] A. Oppenheim and J. Lim. The importance of phase in signals. *Proceedings of the IEEE*, 69:529–541, 1981. 1
- [22] J. Pan, Z. Hu, Z. Su, H.-Y. Lee, and M.-H. Yang. Soft-segmentation guided object motion deblurring. In *Proc. IEEE Conf. Comp. Vis. Patt. Recogn.*, pages 459–468, 2016. 1, 2, 3
- [23] J. Pan, Z. Hu, Z. Su, and M.-H. Yang. Deblurring text images via l0-regularized intensity and gradient prior. In *Proc. IEEE Conf. Comp. Vis. Patt. Recogn.*, pages 2901–2908, 2014. 1
- [24] J. Pan, R. Liu, Z. Su, and X. Gu. Kernel estimation from salient structure for robust motion deblurring. *Signal Processing: Image Communication*, 28(9):1156–1170, 2013. 2

- [25] J. Pan, D. Sun, H. Pfister, and M.-H. Yang. Blind image deblurring using dark channel prior. In *Proc. IEEE Conf. Comp. Vis. Patt. Recogn.*, pages 1628–1636, 2016. 1, 2, 6, 7, 8
- [26] J. Pan, D. Sun, H. Pfister, and M.-H. Yang. Deblurring images via dark channel prior. *IEEE Trans. Pattern Anal. Mach. Intell.*, 2017. 16, 17, 18, 19
- [27] L. Pan, Y. Dai, M. Liu, and F. Porikli. Simultaneous stereo video deblurring and scene flow estimation. In *Proc. IEEE Conf. Comp. Vis. Patt. Recogn.*, July 2017. 1, 3
- [28] G. Papari and N. Petkov. Edge and line oriented contour detection: State of the art. *Image and Vision Computing*, 29(2-3):79–103, 2011. 1
- [29] A. Sellent, C. Rother, and S. Roth. Stereo video deblurring. In *Proc. Eur. Conf. Comp. Vis.*, pages 558–575. Springer, 2016. 1, 3
- [30] J. Shi, L. Xu, and J. Jia. Discriminative blur detection features. In *Proc. IEEE Conf. Comp. Vis. Patt. Recogn.*, pages 2965–2972, 2014. 5
- [31] J. Sturm, N. Engelhard, F. Endres, W. Burgard, and D. Cremers. A benchmark for the evaluation of rgb-d slam systems. In *IEEE/RSJ International Conference on Intelligent Robots and Systems*, pages 573–580, 2012. 7, 8, 13
- [32] S. Su, M. Delbracio, J. Wang, G. Sapiro, W. Heidrich, and O. Wang. Deep video deblurring for hand-held cameras. In *Proc. IEEE Conf. Comp. Vis. Patt. Recogn.*, July 2017. 3
- [33] J. Sun, W. Cao, Z. Xu, and J. Ponce. Learning a convolutional neural network for non-uniform motion blur removal. In *Proc. IEEE Conf. Comp. Vis. Patt. Recogn.*, pages 769–777, 2015. 1, 2, 3
- [34] L. Sun, S. Cho, J. Wang, and J. Hays. Edge-based blur kernel estimation using patch priors. In *Proc. IEEE Int. Conf. Computational Photography*, 2013. 2
- [35] X. Tao, H. Gao, X. Shen, J. Wang, and J. Jia. Scale-recurrent network for deep image deblurring. In *Proc. IEEE Conf. Comp. Vis. Patt. Recogn.*, June 2018. 1, 2, 3, 16, 17, 18, 19
- [36] O. Veksler. Stereo matching by compact windows via minimum ratio cycle. In *Computer Vision, 2001. ICCV 2001. Proceedings. Eighth IEEE International Conference on*, volume 1, pages 540–547. IEEE, 2001. 6
- [37] O. Whyte, J. Sivic, A. Zisserman, and J. Ponce. Non-uniform deblurring for shaken images. *Int. J. Comp. Vis.*, 98(2):168–186, 2012. 7, 8
- [38] J. Wulff and M. J. Black. Modeling blurred video with layers. In *Proc. Eur. Conf. Comp. Vis.*, pages 236–252. Springer, 2014. 3
- [39] L. Xu and J. Jia. Two-phase kernel estimation for robust motion deblurring. In *Proc. Eur. Conf. Comp. Vis.*, pages 157–170. Springer, 2010. 2
- [40] L. Xu and J. Jia. Depth-aware motion deblurring. In *Proc. IEEE Int. Conf. Computational Photography*, pages 1–8, 2012. 1
- [41] L. Xu, C. Lu, Y. Xu, and J. Jia. Image smoothing via l0 gradient minimization. *ACM Trans. Graph.*, 30:174:1–174:12, 2011. 6
- [42] L. Xu, X. Tao, and J. Jia. Inverse kernels for fast spatial deconvolution. In *Proc. Eur. Conf. Comp. Vis.*, pages 33–48. Springer, 2014. 1
- [43] L. Xu, S. Zheng, and J. Jia. Unnatural l0 sparse representation for natural image deblurring. In *Proc. IEEE Conf. Comp. Vis. Patt. Recogn.*, pages 1107–1114, 2013. 1, 2, 6, 7, 8
- [44] Y. Yan, W. Ren, Y. Guo, R. Wang, and X. Cao. Image deblurring via extreme channels prior. In *Proc. IEEE Conf. Comp. Vis. Patt. Recogn.*, pages 6978–6986, 2017. 1, 2, 7, 8, 16, 17, 18, 19
- [45] J. Zhang, J. Pan, J. Ren, Y. Song, L. Bao, R. W. Lau, and M.-H. Yang. Dynamic scene deblurring using spatially variant recurrent neural networks. In *Proc. IEEE Conf. Comp. Vis. Patt. Recogn.*, June 2018. 3
- [46] S. Zheng, L. Xu, and J. Jia. Forward motion deblurring. In *Proc. IEEE Int. Conf. Comp. Vis.*, December 2013. 1, 2

Appendix

A. Method

A.1. Blur Model

Our goal is to find the latent sharp image from a single blurry image. The blurry image can be modeled as a convolution of the latent image with a blur kernel,

$$\mathbf{B} = \mathbf{L} \otimes \mathbf{k}, \quad (6)$$

where $\mathbf{B} \in \mathcal{R}^{m \times n}$, the blurry image is known, $\mathbf{L} \in \mathcal{R}^{m \times n}$ denotes the latent sharp image, and \mathbf{k} is the blur kernel, \otimes is the convolution operator. In the Fourier domain, this corresponds to $\mathcal{F}(\mathbf{B}) = \mathcal{F}(\mathbf{L}) \odot \mathcal{F}(\mathbf{k})$, where \odot represents component-wise multiplication.

A.2. Fourier theory of phase-only images and de-blurring

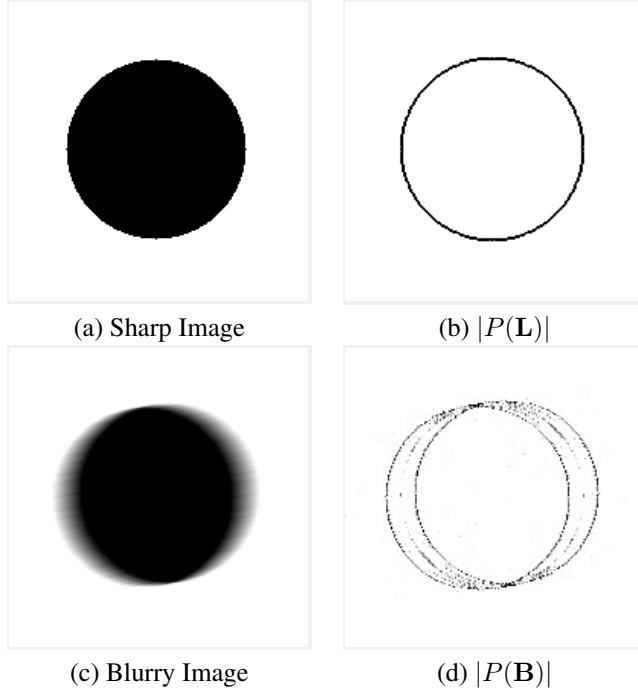


Figure 9. We use a circle image as an example. The image is blurred by a linear kernel, where the kernel length is 20 pixels and the direction is 10 degree.

The phase and amplitude of a complex number $ke^{i\theta}$ are $e^{i\theta}$ and $k \geq 0$ respectively. Applying these component-by-component to a Fourier transformed image $\mathcal{F}(\mathbf{L})$ gives the phase and amplitude components. We denote taking the phase of a complex signal by $\mathcal{P}(\cdot)$. Taking the inverse Fourier transform of the phase-component gives the *phase-only image*, $P(\mathbf{L}) = \mathcal{F}^{-1}(\mathcal{P}(\mathcal{F}(\mathbf{L})))$. It is well known that the phase-only image bears more similarity to the original

image than the analogously defined amplitude image. Figures 9 and 12 show phase-only images derived from real and synthetic images. As may be observed, taking a phase-only image acts as a sort of edge-extractor. This is related to the fact, noted by Kovessy ([13]) that the Fourier components of an edge tend to be in-phase with each other. For a real image \mathbf{L} , the phase-only image will also be real. Another simple property is *rotation-covariance*: if R represents rotation then $P(R(\mathbf{L})) = R(P(\mathbf{L}))$. It is also shift-covariant.

We now make a basic observation regarding the phase-only image of a convolution.

lemma 2. *The phase-only image of a convolution, $P(\mathbf{L} \otimes \mathbf{k})$, is equal to the convolution of the phase-only image and the phase-only kernel.*

$$P(\mathbf{L} \otimes \mathbf{k}) = \mathcal{F}^{-1}(\mathcal{P}(\mathcal{F}(\mathbf{L} \otimes \mathbf{k}))) = P(\mathbf{L}) \otimes P(\mathbf{k}). \quad (7)$$

This results from a simple calculation.

B. Phase-only image of a linear kernel

For a simple linear (straight-line) blur kernel, the form of $P(\mathbf{k})$ can be computed. By rotation and shift covariance, it may be assumed without loss of generality, that \mathbf{k} is axis-aligned, in which case $\mathbf{k}(x, y) = \delta(y)H(x)$, where $\delta(y)$ is a Dirac delta function and $H(x)$ is a top-hat. The Fourier transform is separable, so it follows that $P(\mathbf{k}) = \delta(y)P(H)$. Hence, we investigate what the 1D phase-only signal $P(H)$ is. The result is shown in Figures 10 and 11.

A formula for the shape of the phase-only top-hat of width s (for continuous Fourier Transform) is as follows:

$$P(H_s) = \frac{\sqrt{2\pi}}{s} \frac{\text{sinc}(\pi x/s)}{\cos(\pi x/s)}. \quad (8)$$

The plot of this function is shown in Fig. 13.

Derivation of Equation (8) To compute $P(H) = \mathcal{F}^{-1}(\mathcal{P}(\mathcal{F}(H)))$, we need to find the inverse Fourier transform of the function $h(\omega) = \mathcal{P}(\mathcal{F}(H))$, shown in Fig. 10 (right).

Define $H_s(x)$ to be the top-hat function of width s , defined as $H_s(x) = H(x/s)$, where

$$H(x) = \begin{cases} 1 & \text{if } -1/2 \leq x \leq 1/2 \\ 0 & \text{otherwise} \end{cases}. \quad (9)$$

(This is the function also called the **HeavisidePi** function in Mathematica.) The Fourier transform of $H(x/s)$ is given by⁴

$$\mathcal{F}(H_s) = \frac{s \text{sinc}(s\omega/2)}{\sqrt{2\pi}}.$$

⁴ We follow Mathematica in normalizing the Fourier transform by division by $\sqrt{2\pi}$, so that the Fourier transform and its inverse have the same normalization factor.

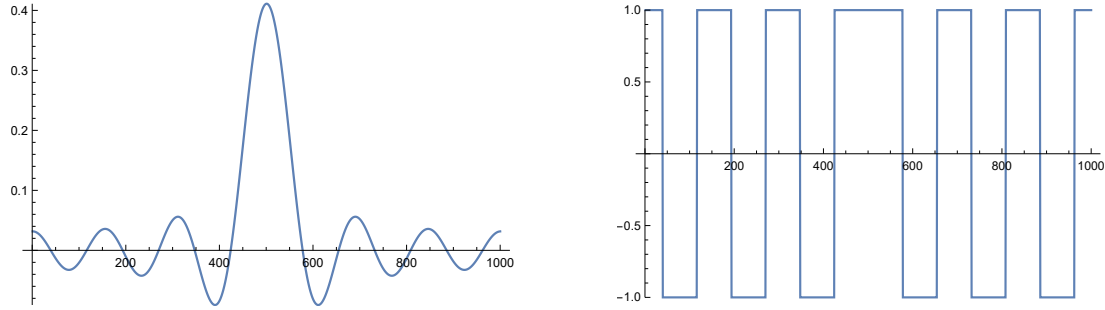


Figure 10. Fourier transform of a top-hat function is sinc (left). The phase of this is shown on right. (The central peak has twice the width of the others. Note that since the top-hat is symmetric, its Fourier transform is real, hence its phase is either $+1$ or -1 .) The phase-only image of the top-hat is obtained by taking the inverse Fourier transform of the function on the right.

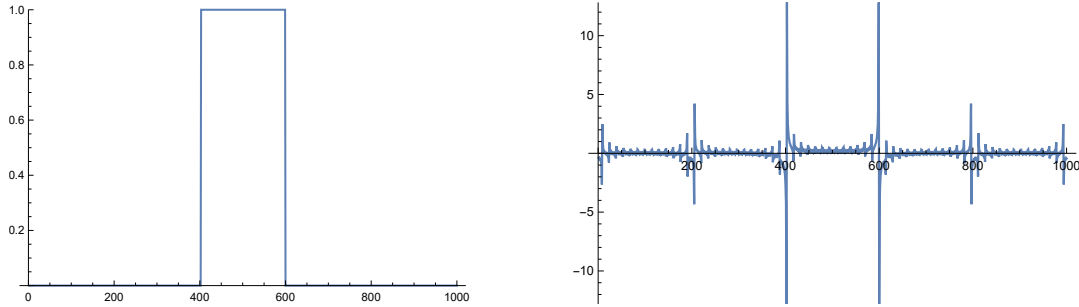


Figure 11. Given a top-hat function (left), the phase-only signal has peaks separated by the width of the top-hat. The principal (central) peaks have the largest amplitude. (Note: to given most visually clear results, the top-hat functions used here and in Fig. 10 are of different width.)

Its phase is

$$h(\omega) = \frac{\text{sinc}(s\omega/2)}{|\text{sinc}(s\omega/2)|},$$

which is shown in Fig. 10 (right). The width of the central step is $4\pi/s$, and the others have width $2\pi/s$, alternating positive and negative. To make the positive and negative steps cancel, we shift by π/s in opposite directions and add:

$$h(\omega - \pi/s) + h(\omega + \pi/s) = 2H(\omega s/(2\pi)).$$

Now, taking inverse Fourier transforms of both sides gives

$$(e^{ix\pi/s} + e^{-ix\pi/s})\mathcal{F}^{-1}(h(\omega)) = \frac{2\sqrt{2\pi}}{s} \text{sinc}(\pi x/s).$$

and finally

$$P(H_s) = \mathcal{F}^{-1}(h(\omega)) = \frac{\sqrt{2\pi}}{s} \frac{\text{sinc}(\pi x/s)}{\cos(\pi x/s)}.$$

□ This may also be rewritten using the following series expansion:

$$\frac{\text{sinc}(\pi x/s)}{\cos(\pi x/s)} = \frac{2s}{\pi^2} \sum_{i=1}^{\infty} \frac{1}{2i-1} \left(\frac{1}{x+z_i} - \frac{1}{x-z_i} \right). \quad (10)$$

where $z_i = (2i-1)s/2$, the zeros of $\cos(\pi x/s)$. Thus, $P(H_s)$ is equal to a sum of simple poles at each z_i with residues proportional to $-1/z_i$.

Derivation of Equation (10). It is sufficient to prove this in the case where $s = 1$. We start with the Weierstrass product formula⁵ for $\cos(\pi x)$:

$$\cos(\pi x) = \prod_{i=1}^{\infty} \left(1 - (x/z_i)^2 \right) = \prod_{i=1}^{\infty} \frac{z_i^2 - x^2}{z_i^2}.$$

Taking absolute values and logarithms gives

$$\log |\cos(\pi x)| = \sum_{i=1}^{\infty} \log \left(\frac{|x^2 - z_i^2|}{z_i^2} \right).$$

Now, taking derivatives of both sides gives

$$\begin{aligned} -\pi \tan(\pi x) &= \sum_{i=1}^{\infty} \frac{2x}{x^2 - z_i^2} \\ &= -\sum_{i=1}^{\infty} \frac{x}{z_i} \left(\frac{1}{x+z_i} - \frac{1}{x-z_i} \right). \end{aligned}$$

Dividing both sides by $-\pi^2 x$ and recalling that $(2i-1)/2 = z_i$, this easily may be rearranged to obtain Equation (10), with $s = 1$. □

⁵ See for instance:

https://en.wikipedia.org/wiki/Weierstrass_factorization_theorem where this formula is given.

Combining Equation (8) and Equation (10) leads to

$$P(H_s) = \mathcal{F}^{-1}(h(\omega)) \\ = \frac{2\sqrt{2}}{\pi^{3/2}} \sum_{i=1}^{\infty} \frac{1}{2i-1} \left(\frac{1}{x+z_i} - \frac{1}{x-z_i} \right). \quad (11)$$

So, $P(H_s)$ is equal to a sum of simple poles with weights proportional to $\pm 1/(2i-1)$ at the zeros z_i of $\cos(\pi x/s)$. This is to be compared with the plot in Fig. 13, and also with Fig. 11 in which the discrete Fourier transform is shown.

[An interesting fact arises from evaluating Equation (10) when $x = 0$. In this case, the equation reduces to the well-known formula for the sum of reciprocals of odd squares:

$$1 = \frac{2s}{\pi^2} \sum_{i=1}^{\infty} \frac{1}{2i-1} \cdot \frac{4}{s(2i-1)}$$

from which

$$\sum_{i=1}^{\infty} \frac{1}{(2i-1)^2} = \frac{\pi^2}{8}.$$

] In order better to visualize what convolution with this function means, we observe that

$$P(H(x/s)) = \frac{2\sqrt{2}}{\pi^{3/2}} \frac{d}{dx} \left(\sum_{i=1}^{\infty} \frac{1}{2i-1} (\log(|x+z_i|) - \log(|x-z_i|)) \right). \quad (12)$$

Ignoring the constant factor, this function may be approximated by

$$P(H(x/s)) \approx \frac{d}{dx} \left(\sum_{i=1}^{\infty} \frac{1}{2i-1} (\delta(x-z_i) - \delta(x+z_i)) \right),$$

where δ is the Dirac delta function. (This approximation is rough, but serves to visualize what is happening.) We denote the bracketed quantity by

$$\sigma(x) = \sum_{i=1}^{\infty} \frac{1}{2i-1} (\log(|x+z_i|) - \log(|x-z_i|)) \\ \approx \sum_{i=1}^{\infty} \frac{1}{2i-1} (\delta(x-z_i) - \delta(x+z_i)). \quad (13)$$

Now, let $\mathbf{B} = \mathbf{L} \otimes \mathbf{k}$, where \mathbf{k} is a straight-line filter $\mathbf{k}(x, y) = H(x)\delta(y)$. For simplicity of notation, we represent this kernel as $H \times \delta$. More generally, $(f \times g)(x, y)$ is defined as $f(x)g(y)$. Then

$$P(\mathbf{B}) = P(\mathbf{L}) \otimes P(\mathbf{k}) \\ = P(\mathbf{L}) \otimes (P(H) \times \delta) \\ = P(\mathbf{L}) \otimes (D_x \sigma \times \delta) \\ = D_x P(\mathbf{L}) \otimes (\sigma \times \delta), \quad (14)$$

where D_x represents the derivative in the x direction (or more generally the direction of alignment of the filter). We summarize.

theorem 1. If $\mathbf{B} = \mathbf{L} \otimes \mathbf{k}$, where $\mathbf{k} = H \times \sigma$ is a straight-line blur kernel, then

$$P(\mathbf{B}) = D_x P(\mathbf{L}) \otimes (\sigma \times \delta),$$

where D_x represents the gradient in the kernel direction. According to the formula Equation (13), this may be approximated as several shifted and weighted copies of $D_x P(\mathbf{L})$ in the direction of the blur.

In other words, blurring with a straight-line filter results in the creation of multiple copies (“ghosts”), of the derivative of the phase-only image, $D_x P(\mathbf{L})$, separated by the width of the filter. (The copies due to the principal peaks will be the most noticeable.)⁶ This is shown in Fig. 4.

Autocorrelation. As was shown, doing phase-only to obtain $P(\mathbf{B})$ from a blurry image results in multiple (two principal) shifted copies of $P(\mathbf{L})$. Note that $P(\mathbf{L})$ is not known. However, this suggests the use of autocorrelation of $P(\mathbf{B})$. There should be two peaks (separated by the width of the blur-kernel) in the autocorrelation image.

Autocorrelation of a signal \mathbf{I} (1 or 2-dimensional) is computed using Fourier transform as:

$$\mathcal{A}(\mathbf{I}) = \mathcal{F}^{-1}(\mathcal{F}(\mathbf{I}) \odot \overline{\mathcal{F}(\mathbf{I})}).$$

Unfortunately, if \mathbf{I} is itself a phase-only image, derived from \mathbf{J} , then

$$\mathcal{F}(\mathbf{I}) = \mathcal{F}(\mathcal{F}^{-1} \mathcal{P}(\mathcal{F}(\mathbf{J}))) = \mathcal{P}(\mathcal{F}(\mathbf{J})).$$

So

$$\mathcal{A}(\mathbf{I}) = \mathcal{F}^{-1}(\mathcal{P}(\mathcal{F}(\mathbf{J})) \odot \overline{\mathcal{P}(\mathcal{F}(\mathbf{J}))}) = \mathcal{F}^{-1}(1) = \delta$$

where δ is a Dirac delta function at the origin. In other words, a phase-only image is **completely un-selfcorrelated**.

In other words, we cannot derive any information whatever from the autocorrelation of a phase-only image. The solution is to use the absolute value of the phase-only image instead. In other words, we compute $\mathcal{A}(|P(\mathbf{B})|)$, which should show the desired behaviour.

Figure 12 show the autocorrelated phase-only image $\mathcal{A}(|P(\mathbf{B})|)$ for various synthetically and naturally blurred images, blurred by camera shake.

C. Sample Application

The TUM RGB-D dataset is a real dataset for man-made scene provided in [31]. We mainly work on the *blur sequence* in the dataset composed of color images of size 640×480 . The TUM dataset does not include ground-truth sharp images.

To show its effectiveness on improving the results of other subsequent tasks, we perform a detailed analysis on visual SLAM on the TUM ‘Teddy’ dataset (see Fig. 14). In particular, we evaluate the ORB-SLAM2 algorithm with the default parameter settings on

⁶ A more exact statement is that $P(\mathbf{B})$ consists of multiple ghosts, separated by the filter width, of the **gradient** of $P(\mathbf{L})$ in the filter direction. An exact derivation is given in the supplementary material. This includes also an exact derivation of $P(H)$.

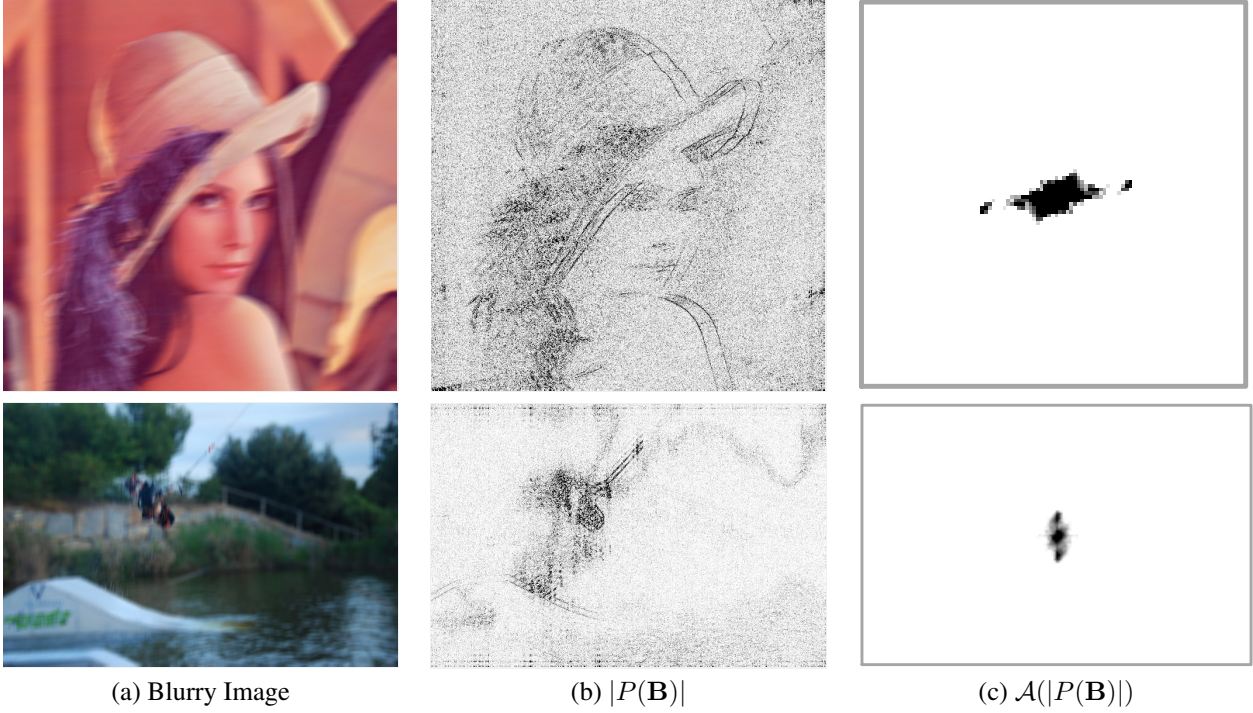


Figure 12. (a) Input blurry images, the top one is synthetic and the bottom one is real. (b) The phase-only $|P(\mathbf{B})|$ of the blurry images results in two principal copies (others more faint) of $P(\mathbf{L})$. (c) Autocorrelation of phase-only blurred images, showing two distinct peaks (separated by the length of the filter kernel). Distinguishing the two principal peaks of the autocorrelation (apart from the origin) can be used to determine the orientation and width of a linear (straight-line) blur kernel.

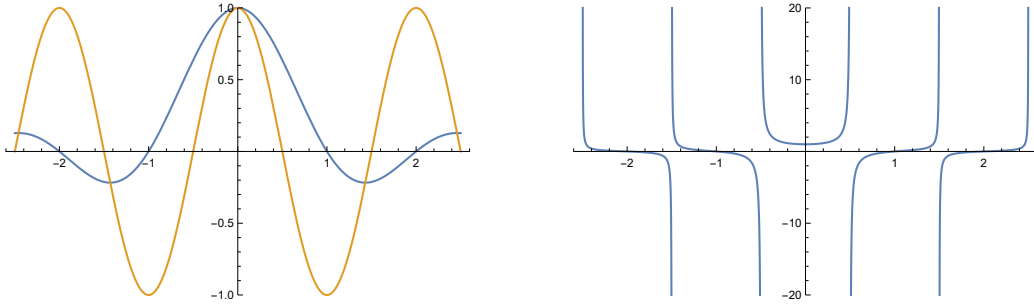
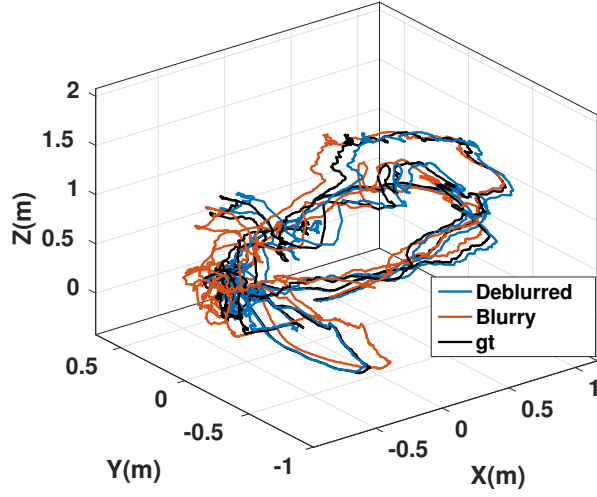


Figure 13. **Left:** Plots of $\text{sinc}(x)$ and $\cos(x)$. The zeros of sinc and \cos alternate. **Right:** Plot of $P(H) = \text{sinc}(\pi x) / \cos(\pi x)$.

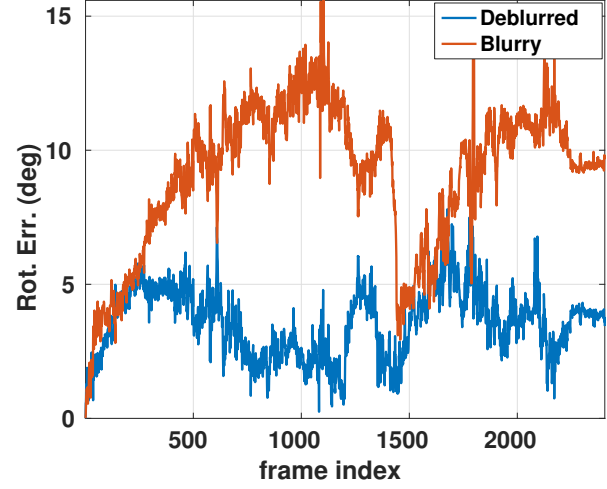
the original image sequence with blurry frames and our deblurred one respectively. Experimental results show that ORB-SLAM2 can achieve better camera pose estimation and extract more feature points for each frame on the deblurred sequence by our single-image deblurring algorithm than the original blurry one.

D. More results

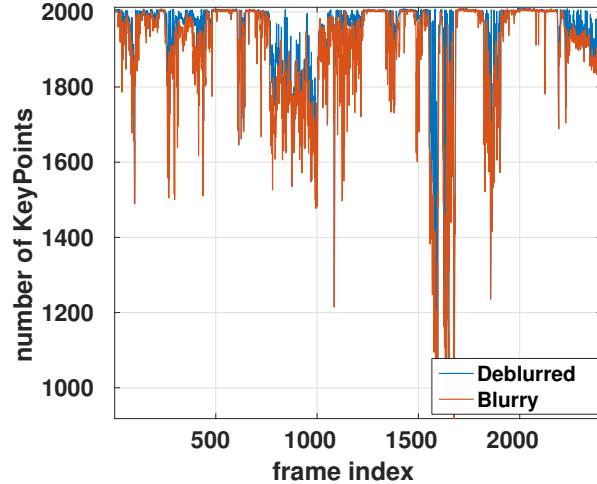
We provide additional experimental evaluation of our method on dataset from [12], shown in Fig.15-18.



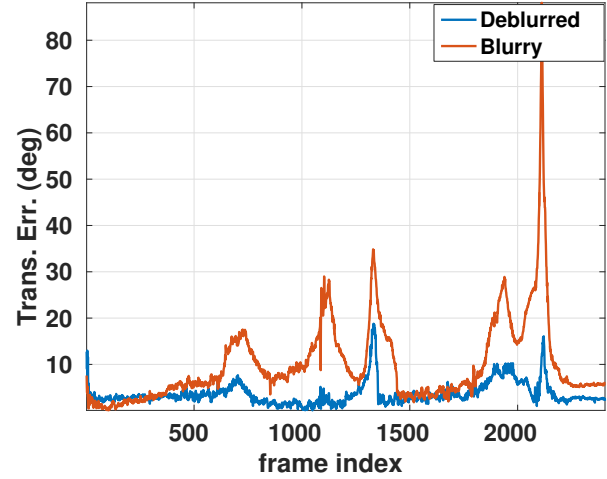
(a) 3D trajectories



(c) Rotation errors (deg.)



(b) Number of feature points

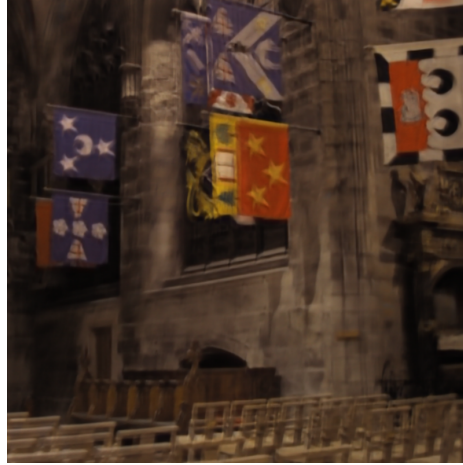


(d) Translation errors (deg.)

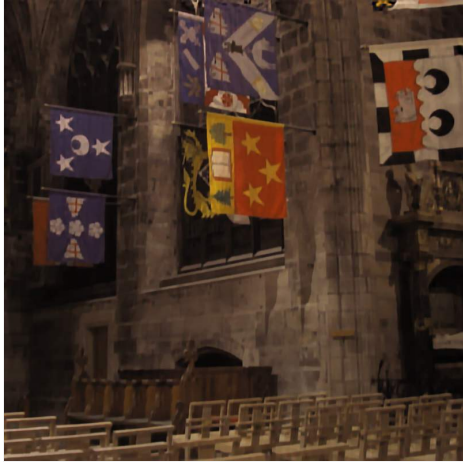
Figure 14. SLAM results on dataset [41] using state-of-the-art ORB-SLAM2 [19]. (a) The estimated 3D camera trajectories using our deblurred images, original blurry images and ground-truth. (b) Number of detected keypoints per frame. (c), (d) Rotational and translational estimation errors using our deblurred images and the original blurry images, respectively.



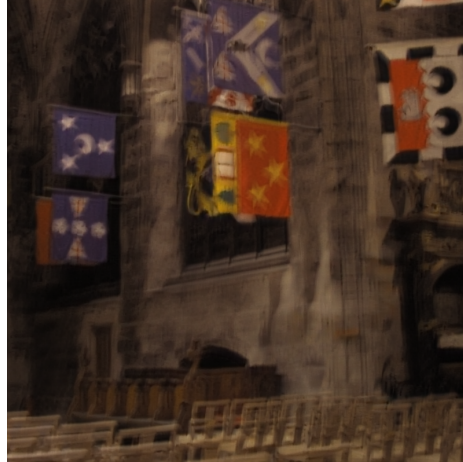
(a) Blurry Image



(b) Tao [35]



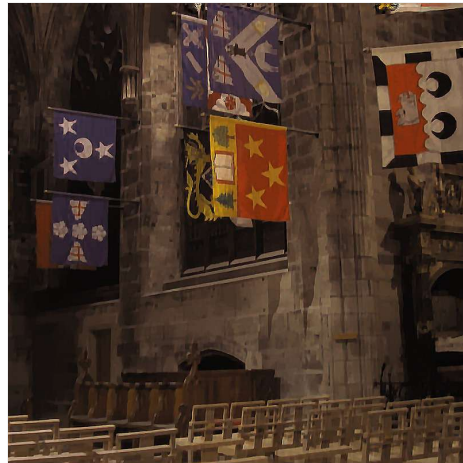
(c) Pan [26]



(d) Nah [20]



(e) Yan [44]

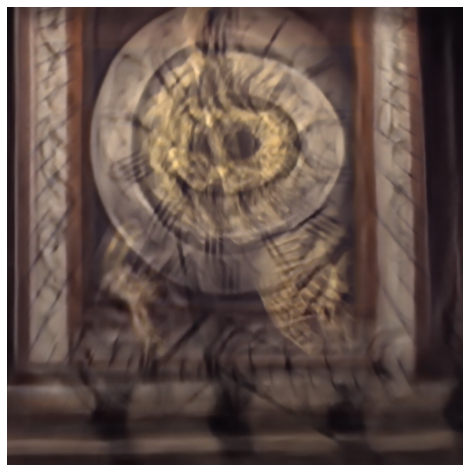


(f) Ours

Figure 15. Example of deblurring result on [12] dataset with kernel estimated by our method. (a) Input blurry images. (b) Deblurring results of [35]. (c) Deblurring results of [26]. (d) Deblurring results of [20]. (e) Deblurring results of [44]. (f) Our deblurring result. (Best viewed on screen).



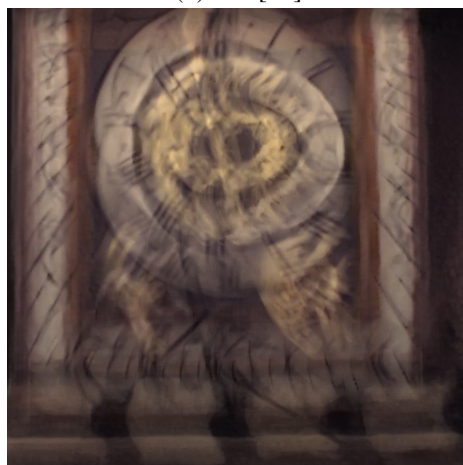
(a) Blurry Image



(b) Tao [35]



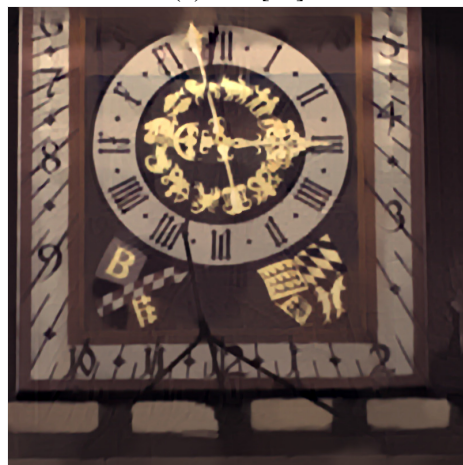
(c) Pan [26]



(d) Nah [20]



(e) Yan [44]



(f) Ours

Figure 16. Example of deblurring result on [12] dataset with kernel estimated by our method. (a) Input blurry images. (b) Deblurring results of [35]. (c) Deblurring results of [26]. (d) Deblurring results of [20]. (e) Deblurring results of [44]. (f) Our deblurring result. (Best viewed on screen).



(a) Blurry Image



(b) Tao [35]



(c) Pan [26]



(d) Nah [20]



(e) Yan [44]



(f) Ours

Figure 17. Example of deblurring result on [12] dataset with kernel estimated by our method. (a) Input blurry images. (b) Deblurring results of [35]. (c) Deblurring results of [26]. (d) Deblurring results of [20]. (e) Deblurring results of [44]. (f) Our deblurring result. (Best viewed on screen).



(a) Blurry Image



(b) Tao [35]



(c) Pan [26]



(d) Nah [20]



(e) Yan [44]



(f) Ours

Figure 18. Example of deblurring result on [12] dataset with kernel estimated by our method. (a) Input blurry images. (b) Deblurring results of [35]. (c) Deblurring results of [26]. (d) Deblurring results of [20]. (e) Deblurring results of [44]. (f) Our deblurring result. (Best viewed on screen).